Title

Mutations in the Spliceosome Component CWC27 Cause Retinal Degeneration with or without Additional Developmental Anomalies.

Journal

American Journal of Human Genetics, 100(4)

Authors

Xu, Mingchu

Xie, Yajing

Abouzeid, Hana

et al.

Publication Date

2017-04-06

DOI

10.1016/j.ajhg.2017.02.008

Peer reviewed

ARTICLE

Mutations in the Spliceosome Component *CWC27* Cause Retinal Degeneration with or without Additional Developmental Anomalies

Mingchu Xu,[1,2,26] Yajing (Angela) Xie,[3,26] Hana Abouzeid,[4,26] Christopher T. Gordon,[5,6,26] Alessia Fiorentino,[7,26] Zixi Sun,[8,26] Anna Lehman,[9] Ihab S. Osman,[10] Rachayata Dharmat,[1,2] Rosa Riveiro-Alvarez,[11,12] Linda Bapst-Wicht,[4] Darwin Babino,[13] Gavin Arno,[7,14] Virginia Busetto,[5,15] Li Zhao,[1,2,16] Hui Li,[8] Miguel A. Lopez-Martinez,[11,12] Liliana F. Azevedo,[4] Laurence Hubert,[6,17] Nikolas Pontikos,[7,18] Aiden Eblimit,[1,2] Isabel Lorda-Sanchez,[11,12] Valeria Kheir,[4] Vincent Plagnol,[18] Myriam Oufadem,[5,6] Zachry T. Soens,[1,2] Lizhu Yang,[8] Christine Bole-Feysot,[6,19] Rolph Pfundt,[20] Nathalie Allaman-Pillet,[4] Patrick Nitschké,[6,21] Michael E. Cheetham,[7] Stanislas Lyonnet,[5,6,22] Smriti A. Agrawal,[1,2] Huajin Li,[8] Gaëtan Pinton,[4] Michel Michaelides,[7,14] Claude Besmond,[6,17] Yumei Li,[1,2] Zhisheng Yuan,[8] Johannes von Lintig,[13] Andrew R. Webster,[7,14] Hervé Le Hir,[15] Peter Stoilov,[23] UK Inherited Retinal Dystrophy Consortium, Jeanne Amiel,[5,6,22] Alison J. Hardcastle,[7,27] Carmen Ayuso,[11,12,27] Ruifang Sui,[8,27] Rui Chen,[1,2,27,*] Rando Allikmets,[3,24,27,*] and Daniel F. Schorderet[4,25,27]

Pre-mRNA splicing factors play a fundamental role in regulating transcript diversity both temporally and spatially. Genetic defects in several spliceosome components have been linked to a set of non-overlapping spliceosomopathy phenotypes in humans, among which skeletal developmental defects and non-syndromic retinitis pigmentosa (RP) are frequent findings. Here we report that defects in spliceosome-associated protein CWC27 are associated with a spectrum of disease phenotypes ranging from isolated RP to severe syndromic forms. By whole-exome sequencing, recessive protein-truncating mutations in *CWC27* were found in seven unrelated families that show a range of clinical phenotypes, including retinal degeneration, brachydactyly, craniofacial abnormalities, short stature, and neurological defects. Remarkably, variable expressivity of the human phenotype can be recapitulated in *Cwc27* mutant mouse models, with significant embryonic lethality and severe phenotypes in the complete knockout mice while mice with a partial loss-of-function allele mimic the isolated retinal degeneration phenotype. Our study describes a retinal dystrophy-related phenotype spectrum as well as its genetic etiology and highlights the complexity of the spliceosomal gene network.

Introduction

Pre-mRNA splicing, which removes introns from eukaryotic transcripts, is an essential step in gene expression. Through the generation of numerous alternatively spliced transcript isoforms from the limited set of genes, the splicing process plays a critical role in giving rise to the protein diversity necessary to establish the complex structures and functions found throughout eukaryotes.[1,2] Splicing of pre-mRNA is catalyzed by the spliceosome, a ribonucleoprotein (RNP) complex that is dynamically assembled on each intron and undergoes several rearrangement steps before excising the intron.[3] The core of the spliceosome is formed by five small nuclear RNP (snRNP) particles and proteomic studies have identified more than 150 spliceosomal proteins including snRNP-specific proteins as

[1]Department of Molecular and Human Genetics, Baylor College of Medicine, Houston, TX 77030, USA; [2]Human Genome Sequencing Center, Baylor College of Medicine, Houston, TX 77030, USA; [3]Department of Ophthalmology, Columbia University, New York, NY 10032, USA; [4]Institute for Research in Ophthalmology, 1950 Sion, Switzerland; [5]Laboratory of embryology and genetics of congenital malformations, Institut National de la Santé et de la Recherche Médicale (INSERM) UMR 1163, Institut Imagine, 75015 Paris, France; [6]Paris Descartes-Sorbonne Paris Cité University, Institut Imagine, 75015 Paris, France; [7]UCL Institute of Ophthalmology, University College London, London EC1V 9EL, UK; [8]Department of Ophthalmology, Peking Union Medical College Hospital, Peking Union Medical College, Chinese Academy of Medical Sciences, Beijing 100730, China; [9]Department of Medical Genetics, The University of British Columbia, Vancouver, BC V6H 3N1, Canada; [10]Department of Ophthalmology, Cairo University, Cairo 11562, Egypt; [11]Department of Genetics, Instituto de Investigación Sanitaria – Fundacion Jimenez Diaz (IIS-FJD), 28040 Madrid, Spain; [12]Centros de Investigación Biomédica en Red Enfermedades Raras, Instituto de Salud Carlos III (CIBERER-ISCIII), 28029 Madrid, Spain; [13]Department of Pharmacology, Case Western Reserve University School of Medicine, Cleveland, OH 44106, USA; [14]Moorfields Eye Hospital, London EC1V 2PD, UK; [15]Institut de Biologie de l'ENS (IBENS), CNRS UMR 8197, INSERM U1024, Ecole Normale Supérieure, PSL Research University, 75005 Paris, France; [16]Department of Genomic Medicine, The University of Texas MD Anderson Cancer Center, Houston, TX 77054, USA; [17]Translational Genetics, INSERM UMR 1163, Institut Imagine, 75015 Paris, France; [18]Genetics Institute, University College London, London WC1E 6BT, UK; [19]Genomic Platform, INSERM UMR 1163, Institut Imagine, 75015 Paris, France; [20]Department of Human Genetics, Radboud University Nijmegen Medical Centre, 6525 Nijmegen, the Netherlands; [21]Bioinformatic Platform, INSERM UMR 1163, Institut Imagine, 75015 Paris, France; [22]Service de Génétique, Hôpital Necker-Enfants Malades, Assistance Publique - Hôpitaux de Paris, 75015 Paris, France; [23]Department of Biochemistry and Cancer Institute, Robert C. Byrd Health Sciences Center, West Virginia University, Morgantown, WV 26506, USA; [24]Department of Pathology and Cell Biology, Columbia University, New York, NY 10032, USA; [25]University of Lausanne and Swiss Federal Institute of Technology, 1015 Lausanne, Switzerland
[26]These authors contributed equally to this work
[27]These authors contributed equally to this work
*Correspondence: ruichen@bcm.edu (R.C.), rla22@cumc.columbia.edu (R.A.)
http://dx.doi.org/10.1016/j.ajhg.2017.02.008.

well as miscellaneous non-snRNP splicing factors.[4–7] Though expressed ubiquitously, most spliceosomal genes associated with Mendelian disease have been classified within one of two non-overlapping phenotypic groups, suggesting tissue-specific functional roles. Mutations in splicing factors *TXNL4A* (MIM: 611595),[8] *RBM8A* (MIM: 605313),[9] *SNRPB* (MIM: 182282),[10] *EIF4A3* (MIM: 608546),[11] *EFTUD2* (MIM: 603892),[12] and *SF3B4* (MIM: 605593)[13] cause syndromes mainly involving craniofacial and skeletal abnormalities, while disruptions of another group of spliceosomal genes—*PRPF3* (MIM: 607301),[14] *PRPF31* (MIM: 606419),[15] *PRPF4* (MIM: 607795),[16] *PRPF6* (MIM: 613979),[17] *PRPF8* (MIM: 607300),[18] and *SNRNP200* (MIM: 601664)[19]—lead to non-syndromic retinitis pigmentosa (RP), a restricted disease phenotype primarily affecting the rod photoreceptors. Recent next-generation sequencing approaches have allowed the identification of many of the disease-associated splicing factors listed above, but nevertheless the structural and functional roles of most spliceosome components and their involvement in human disease remain elusive.[20]

Here, by exome sequencing in multiple families and disease modeling of two mouse alleles, we show that the disruption of the spliceosomal gene *CWC27* (MIM: 617170) leads to a spectrum of isolated to syndromic phenotypes. The syndrome features include retinal degeneration, brachydactyly, craniofacial abnormalities, short stature, and neurological defects, with convergence of the two aforementioned non-overlapping spliceosomopathy phenotype groups. This study identifies a role for CWC27 both during early development and in the maintenance of mature tissues and highlights the complexity of spliceosome function.

Materials and Methods

Clinical Examination of Subjects

Subjects underwent ophthalmic evaluations including best correct visual acuity, slit-lamp biomicroscopy, dilated indirect ophthalmoscopy, fundus photography, visual field tests (Octopus), optical coherence tomography (OCT) (Topcon), fundus autofluorescence (Heidelberg HRT II), and electroretinogram (ERG) (RetiPort ERG system, Roland Consult) using corneal "ERGjet" contact lens electrodes. Informed consents were obtained from all the affected individuals or their guardians. All the diagnostic procedures were approved by the local institutional review boards or ethics committees.

Whole-Exome Sequencing and Bioinformatic Analysis

WES for families 1–3 and 5–7 was performed as follows. Pre-capture Illumina libraries were generated as in previous literature.[21–23] The targeted DNA was captured, washed, and recovered using Agilent Hybridization and Wash Kits (Agilent Technologies). WES was performed by capturing the DNA with the NimbleGenSeqCap EZ Hybridization and Wash kit. Captured DNA libraries were sequenced on an Illumina HiSeq 2000 machine (Illumina). After sequencing, the reads were aligned to assembly hg19 of the human genome using BWA v.0.6.1.[24] Base quality recalibration and local realignment was performed by the Genome Analysis Tool Kit v.3.6.[25] Atlas-SNP2 and Atlas-Indel2 were used for variant calling.[26] Variant frequency data were obtained from public and internal control databases including the Exome Aggregation Consortium (ExAC) database,[27] CHARGE consortium,[28] ESP-6500,[29] and 1000 Genomes Project.[30] Autosomal-recessive inheritance pattern was assumed based on pedigrees, so variants with a minor allele frequency higher than 1/200 were filtered out. Unconserved synonymous and deep intronic (distance $>$ 10 bp from exon-intron junctions) variants were also excluded from further analysis. ANNOVAR[31] (v. 06/17/2015) and dbNSFP suite[32] (v.2.9, includes SIFT, PolyPhen-2, LRT, MutationTaster, MutationAssessor, etc.) were used to annotate protein-altering effects. Reported retinal disease-causing variants were detected based on the HGMD professional database (v. 08/15/2016).

For quartet WES of family 4 (both affected individuals and their parents), Agilent SureSelect libraries were prepared from 3 μg of genomic DNA from each individual and sheared with a Covaris S2 Ultrasonicator. Exome capture was performed with the 50 Mb SureSelect Human All Exon kit V3 (Agilent technologies). Sequencing was carried out on a pool of barcoded exome libraries using a SOLiD5500XL instrument (Life Technologies), and 75+35 paired-end sequences were mapped to the reference human genome (GRCh37/hg19 assembly, NCBI) using Mapreads (LifeScope, Life Technologies). Variant calling was performed with SAMtools. Variants were filtered against publicly available SNPs plus variant data from in-house exomes (Institut Imagine).

RT-PCR and Sanger Sequencing of Human RNA

For family 2 RT-PCR, mRNA was isolated from venous blood using the QIAamp RNA Blood Mini Kit (QIAGEN cat# 75142) with a fast spin-column procedure. Genomic DNA was eliminated by on-column treatment with DNase I using the QIAGEN RNase-Free DNase Set (QIAGEN cat# 79254). Complementary DNA synthesis was conducted using oligo(dT) primers, following the thermal cycling conditions in Applied Biosystems TaqMan Reverse Transcription kit (Applied Biosystems cat# N8080234), using an ABI 9700 thermocycler (Applied Biosystems). PCR amplification consisted of 40 cycles of 94°C for 15 s, 65°C for 30 s, and 68°C for 1 min, and 1 cycle of 68°C for 5 min was used for final extension. The primer pair for PCR was designed to encompass *CWC27* exons 5 and 6 (forward: 5′-ACATGTTGCGACTGTCAGAA-3′ and reverse: 5′-ACTTCCTCCTCTGGTTTCTCT-3′).

For family 4 RT-PCR, total RNA was extracted from PAXgene tubes using the PAXgene Blood RNA Kit (Preanalytix, ref. no 762174). RNA was treated with DNase I and retro-transcription performed on 1 μg of total RNA using the Verso cDNA Synthesis Kit (Thermo Scientific). PCRs were performed using 1/20th of the total cDNA and Phusion DNA polymerase (Thermo Scientific) in a total volume of 20 μL with the following program: 98°C for 3 min; 35 cycles of 98°C 10 s, 64°C 15 s, 72°C 25 s; final elongation at 72°C for 2 min. A primer pair mapping to *CWC27* exons 4 and 10 (forward: 5′-TTCTTCACACTGGGTCGAGC-3′ and reverse: 5′-TCCACTTCTCCTTCTCCAGC-3′) was used to evaluate splicing defects. PCR products were cloned into the TOPO Vector using the Zero Blunt TOPO PCR cloning kit (Invitrogen) and were subsequently sequenced with a vector-specific primer.

Phenotyping of *Cwc27*$^{tm1b/tm1b}$ Mice

Heterozygous *Cwc27*$^{tm1b/+}$ couples were bred and pregnant females were euthanized at E12.5, E14.5, E16.5, and E18.5. Embryos were dissected, fixed in 4% PFA for 3 to 5 hr depending on the size

of the embryos, and photographed using a Leica camera coupled with a dissection Leica microscope. OCT was performed on anesthetized mice as described[33] using a Mikron III system (Phoenix Research Labs). Data were analyzed with Stream Pix 6 and Micro OCT V7.242.

Generation of *Cwc27*$^{K338fs/K338fs}$ Mice via the CRISPR-Cas9 System

To target the *Cwc27* exon 11 in mice, the sgRNA 5′-AGAAACTGC CATAAAAGTGG-3′ was designed using the MIT CRISPR design tool. Oligonucleotides containing the *Cwc27* sgRNA target sequence was cloned into pDR274, a cloning vector (Addgene), to form a T7 promoter-mediated sgRNA expression vector. *Bsa*I digestion was performed to linearize the vector. After gel purification (QIAGEN), we used the linearized expression vector as a template to produce sgRNA using the Maxiscript T7 kit (Life Technologies), followed by purification with RNA Clean and Concentrator-25 (Zymo Research). RNA concentration was measured using a NanoDrop ND1000. To make Cas9 mRNA, a modified pX33010 was linearized with NotI and used as template for RNA production (mMESSAGE mMACHINE T7 Transcription Kit, Invitrogen).

Cas9 mRNA (40 ng/μL) was mixed with sgRNA (20 ng/μL) and microinjected into C57BL/6J embryos at the single-cell stage. Once the embryos reached blastocyst stage, they were transferred into the uterus of pseudo-pregnant females to obtain founder mice. Mouse genotyping was performed using PCR and Sanger sequencing with primer pair: CWC27_KO1_F: 5′-CTCGTGTAAAACGACGGC CAGTGGCACTGTGTCAGAACAGGA-3′ and CWC27_KO1_R: 5′-CTGCTCAGGAAACAGCTATGACCACACTTCCTCAGCCAAA CA-3′. All animal operations were approved by the Institutional Animal Care and Use Committee at Baylor College of Medicine.

ERG in Mice

Mice were dark-adapted overnight and then anesthetized with ketamine (22 mg/kg), xylazine (4.4 mg/kg), and acepromazine (0.37 mg/kg) by intraperitoneal injection. Tropicamide (1.0%) and phenylephrine (2.5%) solutions were used to dilate the pupils in red dim light and the cornea was anesthetized with proparacaine (1.0%). Goniosoft (2.5%) was gently applied on the cornea to keep it moistened and enhance the contact between the cornea and the ERG electrode. Scotopic ERG was performed at four flash intensities (0.1, 1, 2.5, 25 cd*s/m^2). The LKC UTAS Visual Diagnostic System and EMWIN software (LKC Technologies) was used to digitize and store the recordings. ERG data were analyzed and plotted with GraphPad Prism5 software (GraphPad). Two-tailed unpaired t test with Welch's correction was performed for each light condition.

Mouse Retina Hematoxylin and Eosin Staining

Mouse eyes were enucleated and fixed overnight at 4°C in fresh Davidson's fixative. Fixed eyes were processed through a series of ethanol dehydration steps (50%, 70%, 95%, and 100%) for 1 hr each. Eyes were then paraffin-embedded for sectioning. Serial paraffin sections (7 μm) were obtained and H&E stained according to standard protocol. H&E-stained slides were visualized using light microscopy (Zeiss Apotome).

Mouse Retina mRNA qRT-PCR

Reverse-transcription PCR reactions were performed on 30 ng of total retinal RNA and were primed with a mixture of oligo-dT and random hexamers. *Cwc27* mRNA qPCR was performed according to the Universal SYBR Green Quantitative PCR Protocol (Sigma-Aldrich) using the *Cwc27* primer pair 5′-ATG CAAGTGCCAGTGTGAAG-3′ (forward) and 5′-TTTCGCTGC TAAGAGTTCTCG-3′ (reverse) and the *Gapdh* primer pair 5′-CATGGCCTTCCGTGTTCCTA-3′ (forward) and 5′-CCTGC TTCACCACCTTCTTGAT-3′ (reverse) as the internal control. Relative mRNA quantity was calculated using the $2^{-\Delta\Delta Ct}$ method as described previously.[34]

Human mRNA qRT-PCR

RNA was extracted from primary fibroblasts of the two affected individuals from family 4 using Tri Reagent (Ambion). Cells of an unaffected individual were used as the control. 5 μg of RNA were treated with 1 μL of Turbo DNase (Ambion) in a final volume of 50 μL. Samples were incubated for 30 min at 37°C. After phenol extraction and RNA precipitation, samples were washed with 70% EtOH and re-suspended in the appropriate volume of H_2O. Reverse transcription was performed on 1 μg RNA using Superscript III (Invitrogen) in a final volume of 20 μL. qPCR was performed in duplicate in a 96-well plate in a Bio-Rad CFX96 Real Time System. 1 μL cDNA and 10 μL of SYBR Select Master Mix (Applied Biosystem) in a final volume of 20 μL were used. Negative controls (no reverse transcriptase or no template) were performed, and no Ct value was detected in either case. Primers mapping to exons 1 and 3 of *CWC27* were used for amplicon qPCR-1 (a region in which *CWC27* splicing is not affected by the mutation in family 4): 5′-ATGAGCAACATCTACATCCAGGAG-3′ (forward) and 5′-CCTTGGACTATGAAACCAGGC-3′ (reverse). Primers mapping to exons 6 and 8 of *CWC27* were used for amplicon qPCR-2 (the forward primer, mapping to exon 6, binds to a region skipped in the affected individuals of family 4): 5′-AAGAAATTGAAACC CAAAGGCAC-3′ (forward) and 5′-CAGAACTGAGATGTGGAT CATCC-3′ (reverse). *GAPDH* primers: 5′-TTAAAAGCAGCCCT GGTGAC-3′ (forward) and 5′-CTCTGCTCCTCCTGTTCGAC-3′ (reverse). Relative mRNA quantity was calculated using the $2^{-\Delta\Delta Ct}$ method as described previously.[34]

Results

Clinical Findings

A total of ten affected individuals from seven unrelated families of diverse ethnicities were studied. The clinical findings of all the affected individuals are summarized in Table 1 and phenotypes of selected individuals are presented in Figure 1. We observed a common phenotype in the majority of these affected individuals, consisting of retinal degeneration (9/10), brachydactyly (9/10), craniofacial defects (8/10), short stature (8/10), and neurological defects (8/10). Clinical description of 2:II-1 and 2:II-2 has been previously reported; however, the genetic etiology was unknown.[35] In our cohort, retinal defects include RP in most affected individuals, with night blindness occurring at around 10 years of age, followed by restriction of visual fields (Figure 1B), while the affected individual 7:II-1 has more severe retinal defects and was diagnosed as Leber congenital amaurosis (LCA). Brachydactyly is a frequent finding, usually occurring in the distal phalanges of digits, with some affected individuals presenting hypoplastic

Table 1. Clinical Phenotypes of Affected Individuals with *CWC27* Mutations

Affected Individual	Age	Age of Dx (Abnormality)	Ethnicity	Craniofacial Defects	Neurological	Brachydactyly	Ocular	Growth	Additional Abnormalities
1:II-3	20	unknown	Yemenite	+	SD; DW (3 yo)	+	RP	SS	cafe-au-lait spots
1:II-4	18	unknown	Yemenite	+	SD; DW (3 yo)	+	RP	SS	cafe-au-lait spots, hallux valgus both sides, flat feet
2:II-1	66	10 (NB)	Spanish	+	moderate ID, PR	+	RP	SS (−2 SDs)	unspecific endocrinological dysfunction
2:II-2	64	10 (NB)	Spanish	+	moderate ID	+	RP	SS (−2 SDs)	unspecific endocrinological dysfunction
3:II-1	14	9 (NB)	Han Chinese	–	–	–	RP	normal	–
4:II-3	17	prenatal (KC)	Moroccan	+	ID; FD; severe PR;	+	flat ERG; altered VEP	SS	alopecia, absent eyebrows and eyelashes, ichthyosis, multiple KC
4:II-4	12	prenatal (IGUR)	Moroccan	+	ID; FD; severe PR; CA	+	flat ERG; altered VEP	SS (−4 SDs, at birth)	alopecia, absent eyebrows and eyelashes, ichthyosis, ectopic testis
5:II-1	23	8 (RP)	Indian	+	ID; SD (6 yo); DW (2 yo); FD (2 yo); ACM type 1	+	RP	SS	neonatal hypotonia, inguinal hernia, bladder cyst, heart murmur
6:II-1	2	at birth (CS)	Indian	+	– (at 19 months)	+	normal at 2 months	SS (−2 SDs, 19 months)	bilateral SVC, 2 large VSDs, horseshoe kidney
7:II-1	7	1 (LCA)	Han Chinese	–	–	+ (mild)	LCA	height: −0.8SD	–

Abbreviations are as follows: ACM, Arnold-Chiari malformation; CA, cortical atrophy; CS, craniosynostosis; DW, delay of walking; Dx, diagnosis; ERG, electroretinogram signals; FD, feeding difficulty; ID, intellectual disability; IUGR, intrauterine growth restriction; KC, kidney cysts; LCA, Leber congenital amaurosis; NB, night blindness; PR, psychomotor retardation; RP, retinitis pigmentosa; SD, speech delay; SD, standard deviation; SS, short stature; SVC, superior vena cava; VEP, visual evoked potential response; VSD, ventricular septal defect; yo, years old.

nails (Figure 1C). Craniofacial anomalies include frontal bossing, large columella, micrognathia, down-slanting palpebral fissures, large and low-set ears, and hypoplasia of nares. Short stature was noted, with height usually being two standard deviations or more below the mean. Neurological features include delays in speech, feeding, and walking as well as intellectual disability. Notably, two affected individuals (3:II-1 and 7:II-1) presented with a retinal phenotype without additional syndromic abnormalities except for a mild brachydactyly in 7:II-1. The affected individual 6:II-1 had not presented with RP at the time of clinical ascertainment at 2 months of age.

Additional family-specific abnormalities were also identified (Table 1). Individuals 1:II-3 and 1:II-4 have café-au-lait spots and 2:II-1 and 2:II-2 show late-onset obesity and unspecific endocrinological dysfunction. Individuals 4:II-3 and 4:II-4 present extensive hair and skin problems including alopecia, absent eyebrows and eyelashes, ichthyosis, eczema, and keratosis. Individuals 5:II-1 and 6:II-1 also have early developmental defects in various organs including bladder, heart, and kidney.

Genetic Findings

WES was performed in these seven families to identify the underlying genetic cause for this phenotype spectrum. After variant filtering and prioritization, biallelic variants in *CWC27*, a gene encoding a spliceosome-associated protein, were identified in all affected individuals. Strikingly, all of the *CWC27* variants are protein truncating (annotation according to GenBank: NM_005869.3). A homozygous stop-gain variant (c.943G>T [p.Glu315*]) was identified in 1:II-3 and 1:II-4 of Yemenite origin. A homozygous synonymous variant (c.495G>A [p.?]) was identified in 2:II-1 and 2:II-2 of Spanish origin.[35] This variant resides at the highly conserved *CWC27* exon 5/intron 5 junction. It was predicted to affect splicing by AdaBoost and Random Forest (score 1.0 for both), which combine the output of seven splice site prediction algorithms.[36] In the

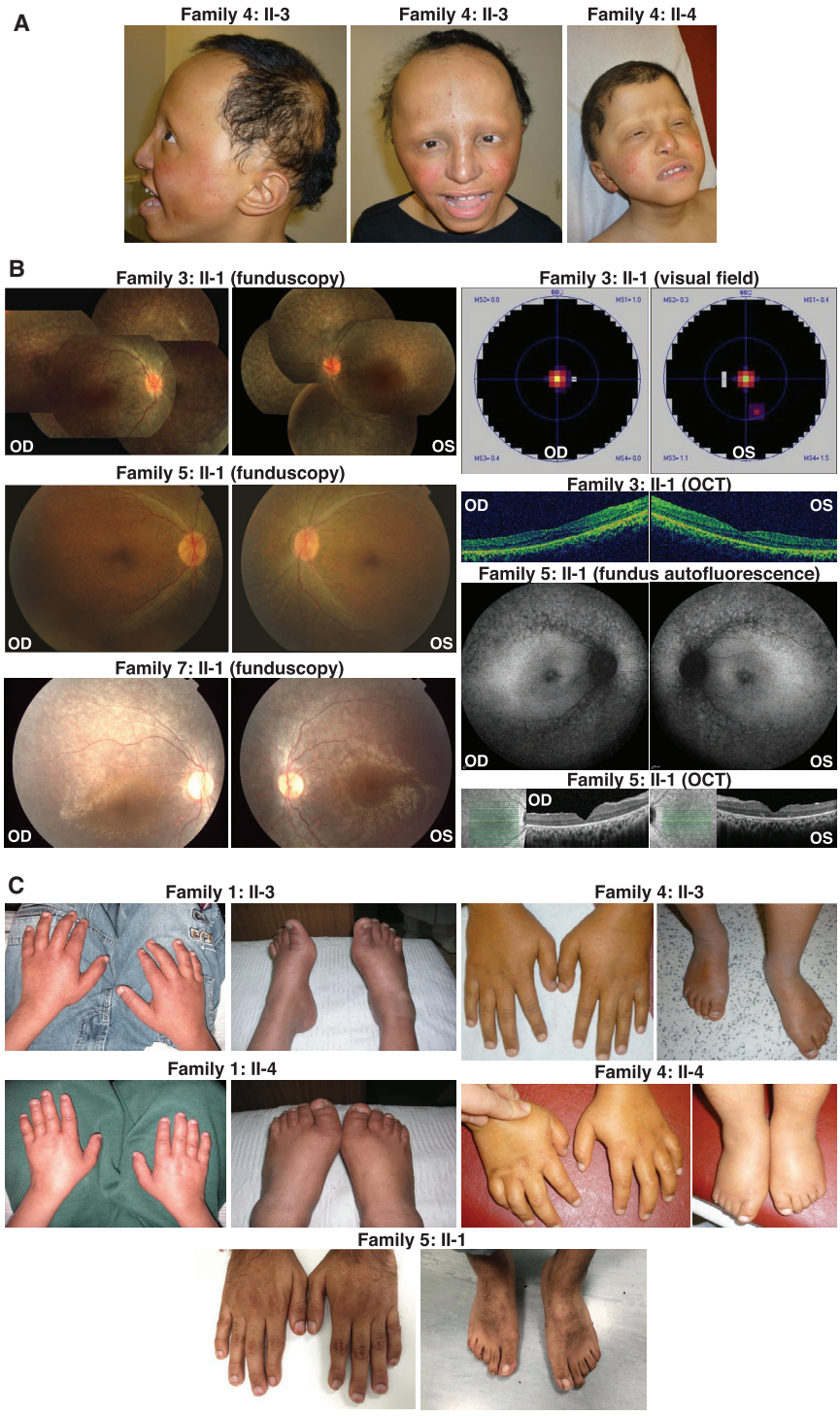

Figure 1. Clinical Findings in This Study
(A) Craniofacial defects of the two affected siblings in family 4. Note the high frontal hairline, sparse hair, eyebrows, and eyelashes, low-set ears, and thick lips.
(B) Retinal phenotypes of affected individuals in families 3, 5, and 7. For individual 3:II-1, funduscopy shows wide-spread grayish and charcoal gray pigment flecks and crumbs in the retina. OCT shows irregular retinal structure with thickening of the fovea and disappearance of the ellipsoid and interdigitation zone. Visual field test shows tunnel vision in both eyes. For individual 5:II-1, funduscopy and fundus autofluorescence imaging show thinning of the retinal vessels and a reduced autofluorescence from the RPE layer consistent with outer retinal degeneration. OCT through the retinal fovea shows a loss of volume of the outer nuclear layer (photoreceptor nuclei) and complete absence of the photoreceptor outer segments throughout the field of view. For individual 7:II-1, funduscopy demonstrates wide-spread salt and pepper pigment changes. Abbreviations are as follows: OCT, optical coherence tomography; OD, oculus dexter, the right eye; OS, oculus sinister, the left eye.
(C) Brachydactyly of affected individuals in families 1, 4, and 5. Note the shortening of the distal phalanges and hypoplastic nails.

non-syndromic Han Chinese RP-affected individual 3:II-1, a homozygous frameshift mutation (c.1002dupA [p.Val335Serfs*13]) was found. This variant is the most C-terminal variant identified in our cohort. Family 4 is from Morocco and a homozygous splicing variant at the exon 6/intron 7 junction (c.599+1G>A [p.?]) was observed in both affected individuals 4:II-3 and 4:II-4. Interestingly, in 5:II-1 and 6:II-1, we identified the same compound heterozygous stop-gain variants in *CWC27* (c.[19C>T];[427C>T], p.[Gln7*];[Arg143*]). In individual 5:II-1, the p.Gln7* mutation is maternal and the p.Arg143* mutation is paternal, while in individual 6:II-1, the parental origin of the alleles is the opposite. Both of the families are of Indian ethnicity but sequence data confirmed they are unrelated. Finally, in 7:II-1, we identified compound heterozygous protein-truncating mutations (c.[617C>A];[1002dupA], p.[Ser206*];[Val335Serfs*13]), of which one (c.1002dupA [p.Val335Serfs*13]) is recurrent in 3:II-1. All of the seven *CWC27* variants identified are absent or occur only once in the heterozygous state in the ExAC and gnomAD databases containing more than 120,000 control individuals (Table S1). In addition, the allele frequency of all *CWC27* protein-truncating variants that affect the longest *CWC27* transcript (GenBank: NM_005869.3) is approximately 1 in 8,000 (gnomAD), strongly supporting *CWC27* as a disease-associated gene for a rare recessive Mendelian phenotype based on Hardy-Weinberg equilibrium. Finally, Sanger sequencing was performed to confirm the mutations and genotype-phenotype co-segregation in these families (Figure 2A).

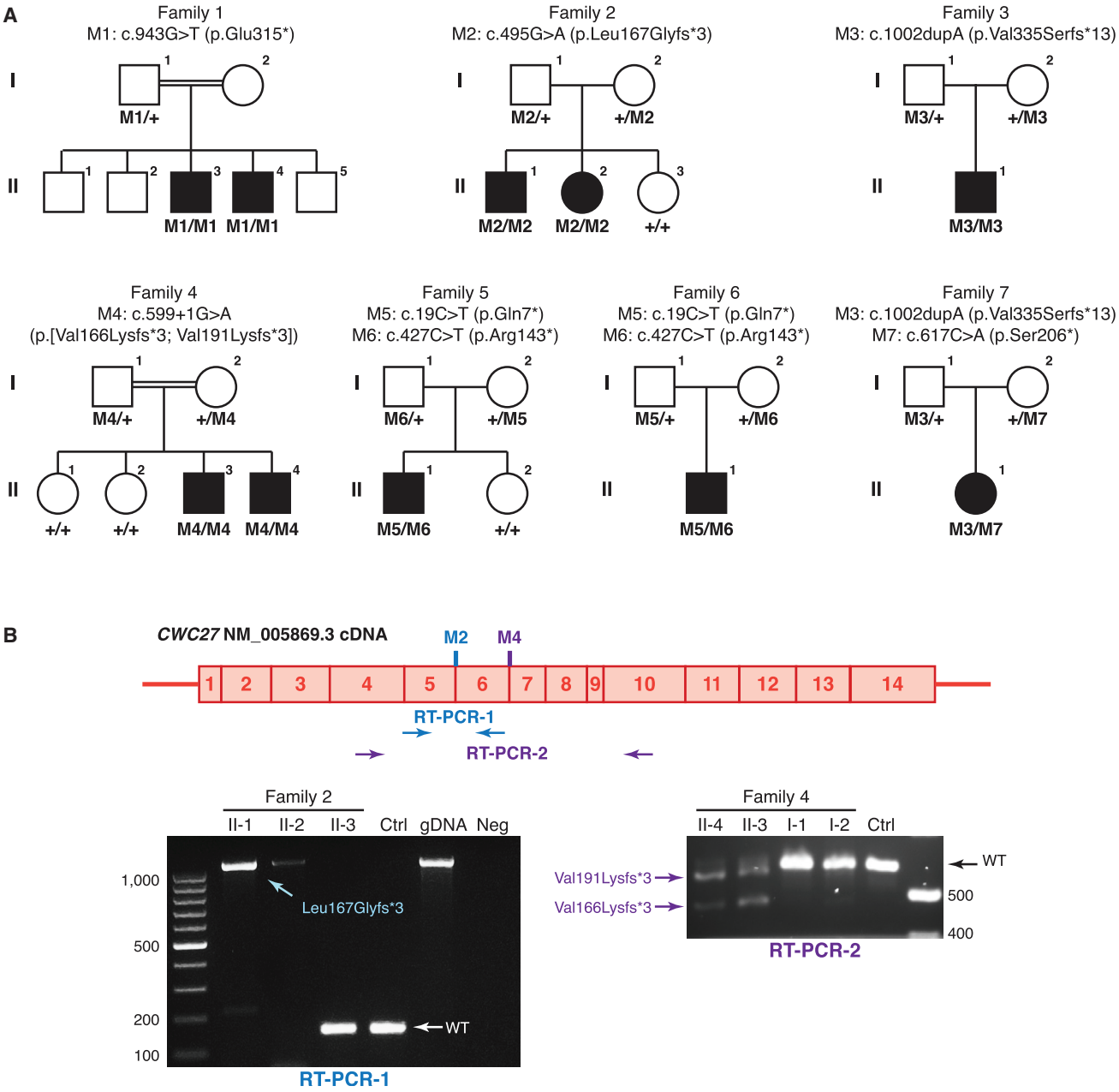

Figure 2. Genetic Findings in This Study

(A) The pedigrees of seven families with recessive *CWC27* mutations. Variant annotations were based on GenBank: NM_005869.3.

(B) RT-PCR confirmed the protein-truncating effects of the two splice-site mutations. RT-PCR-1 in family 2: primer pair spanning *CWC27* exon 5 to exon 6 was used. Both affected individuals show a 1,098 bp PCR product, suggesting complete intron 5 inclusion, whereas control subjects show 154 bp normal size PCR product. Abbreviations are as follows: gDNA, genomic DNA as intron inclusion control; Neg, negative control without templates. RT-PCR-2 in family 4: primer pair spanning *CWC27* exon 4 to exon 10 was used. In individuals 4:II-3 and 4:II-4, two abnormal PCR bands were seen. Sanger sequencing showed the upper band is the result of activation of a cryptic splice site within exon 6, with production of a mature mRNA lacking the final 29 nucleotides of exon 6, leading to the frameshift p.Val191Lysfs*3. The lower band results from complete skipping of exon 6, leading to the frameshift p.Val166Lysfs*3.

To confirm that the two putative splicing-disrupting variants in family 2 and family 4 alter the open reading frame of *CWC27*, we performed RT-PCR analysis on RNA samples derived from the blood of affected individuals. In family 2, a primer pair spanning *CWC27* exons 5 and 6 was used for cDNA and genomic DNA (gDNA) amplification and we observed a non-spliced PCR product of 1,098 bp in 2:II-1 and 2:II-2, while a spliced product of the expected size (154 bp) was detected in 2:II-3 and another control individual (Figure 2B). The size of the PCR product in 2:II-1 and 2:II-2 suggested an inclusion of the entire intron 5 in the mutated *CWC27* transcript, generating a frameshift mutation (p.Leu167Glyfs*3), and this was confirmed by Sanger sequencing of the product. Similarly, in family 4,

the effect of the c.599+1G>A variant on splicing was evaluated. Two abnormal splicing events occurred in the samples of 4:II-3 and 4:II-4 compared with 4:I-1, 4:I-2, and another control subject: one led to the activation of a cryptic splicing site within exon 6 and the other caused complete skipping of exon 6 (Figure 2B). Both splicing changes result in a shift of the reading frame and premature stop codons. Based on the RT-PCR and Sanger sequencing results, the protein-altering effect of the c.599+1G>A variant is annotated as p.[Val191Lysfs*3;Val166Lysfs*3].

Phenotype of *Cwc27* Knockout Mice

To recapitulate the phenotypes of affected individuals, we identified a knockout/reporter mutant of *Cwc27* generated by the Knockout Mouse Phenotyping program (KOMP2) named B6N(Cg)-*Cwc27*$^{tm1b(KOMP)Wtsi}$/J (referred to as tm1b). *Cwc27* exon 3 is deleted in this tm1b allele and a lacZ/transcription termination cassette is inserted downstream of exon 2. After backcrossing this mutant to C57BL/J mice to eliminate the *rd8* allele present in the C57BL/N strain,[37] we analyzed the retina of *Cwc27*$^{tm1b/+}$ mice at P30 and P180 and did not observe any abnormalities. *Cwc27*$^{tm1b/tm1b}$ mice are recorded as pre-weaning lethal by Mouse Genome Informatics (MGI) and we were able to obtain only three *Cwc27*$^{tm1b/tm1b}$ mice out of 56 matings that produced 180 offspring (for Mendelian ratio, see Table S2). Two mice died unexpectedly at P2 and P32, respectively. The third one shows gray hair and growth retardation (Figure 3E) compared with the *Cwc27*$^{tm1b/+}$ control (Figure 3A). OCT and H&E staining at P28 showed that its retina, particularly the photoreceptor layer, is severely dystrophic (Figures 3G and 3H).

In order to investigate when the *Cwc27*$^{tm1b/tm1b}$ mutants are lost, we analyzed the embryos at E12.5, E14.5, E16.5, and E18.5. Seven breedings between *Cwc27*$^{tm1b/+}$ mice generated 57 embryos with a ratio not different from the expected 1:2:1 Mendelian ratio (Table S2). All *Cwc27*$^{tm1b/tm1b}$ embryos showed abnormalities when compared with wild-type (WT) or *Cwc27*$^{tm1b/+}$ embryos (Figures 3I–3L). Specifically, at E12.5, we observed marked growth retardation, neural tube closure failure, and absence of limb buds in *Cwc27*$^{tm1b/tm1b}$ embryos with the most severe defects (Figure 3I). At later stages, additional anomalies were seen in the homozygous mutants such as exencephaly and digit separation delay (Figures 3J–3L). These phenotypes, though much more severe than the human clinical manifestations, demonstrate the delayed growth as well as compromised craniofacial and limb development in the *Cwc27* mutants.

The Mutant Mouse Resource and Research Center (MMRRC) program at University of California, Davis generated another *Cwc27* knockout line *Cwc27*^{tm1Lex} on a different genetic background (129S5/SvEvBrd and C57BL6/J) and *Cwc27* exon 1 is deleted in this tm1Lex allele. The *Cwc27*$^{tm1Lex/tm1Lex}$ mutants also show marked prenatal lethality, with only one surviving *Cwc27*$^{tm1Lex/tm1Lex}$ mouse and eight dead *Cwc27*$^{tm1Lex/tm1Lex}$ embryos identified from breeding (MMRRC). The only postnatal mutant exhibited growth retardation, retinal depigmentation, and numerous neurological, immunological, and blood chemistry abnormalities as recorded by MMRRC.

Characterization of *Cwc27*$^{K338fs/K338fs}$ Mice to Explore Phenotypic Variability

It is striking that the degree of severity of the clinical phenotypes among our affected individuals appears to correlate with the position of the truncating mutation. Specifically, the two affected individuals in families 3 and 7 present with retinal degeneration (RP/LCA) with significantly milder or no extraocular defects. The p.Val335Serfs*13 variant carried by these two affected individuals is the most C-terminal variant identified in this cohort, suggesting that residual CWC27 function may be retained in this scenario. Therefore, to further delineate the *CWC27*-associated genotype-phenotype correlation, we utilized the CRISPR-Cas9 system to generate a second mouse model on the C57BL6/J background targeting *Cwc27* exon 11 to mimic the p.Val335Serfs*13 allele in these two affected individuals (Figure 4A). One allele, c.1011_1018delAAAAGTGG (p.Lys338Glyfs*25) (GenBank: NM_026072.1; referred to as K338fs), with the most similarity to the human mutation was selected for further study. Strikingly, we observed no significant lethality (13:27:12 for WT:*Cwc27*$^{K338fs/+}$:*Cwc27*$^{K338fs/K338fs}$) in *Cwc27*$^{K338fs/K338fs}$ mice. At 6 months of age, the mice underwent retinal phenotyping. ERG showed that the *Cwc27*$^{K338fs/K338fs}$ mice have about 50% reduction of a-wave and b-wave amplitudes compared with *Cwc27*$^{K338fs/+}$ littermates, indicating a compromised retinal function (Figure 4B). H&E staining showed apparent thinning of the outer retina, specifically in the photoreceptor layer (Figure 4C).

Cwc27/*CWC27* mRNA Does Not Undergo Complete Nonsense-Mediated Decay

The absence of lethality observed in *Cwc27*$^{K338fs/K338fs}$ mice strongly suggests that the mouse K338fs allele is hypomorphic compared with the complete null allele in *Cwc27*$^{tm1b/tm1b}$ and *Cwc27*$^{tm1Lex/tm1Lex}$ mice. None of the commercially available CWC27 antibodies were generated using mouse antigen completely N-terminal to the *Cwc27*$^{K338fs/K338fs}$ frameshift site, hindering the possibility to detect residual CWC27-truncated proteins in the mutant mice. Therefore, we performed quantitative RT-PCR in mouse retina RNA and found that the *Cwc27* mRNA level in *Cwc27*$^{K338fs/K338fs}$ mice was 45% of that in WT mice (Figure 5A), indicating that *Cwc27* K338fs mRNA does not undergo complete nonsense-mediated decay (NMD). Furthermore, qRT-PCR on the RNA of the two affected individuals from family 4 showed that the *CWC27* mRNA quantity was reduced by only 33%–43% compared with a control subject (Figure 5B). The mRNA

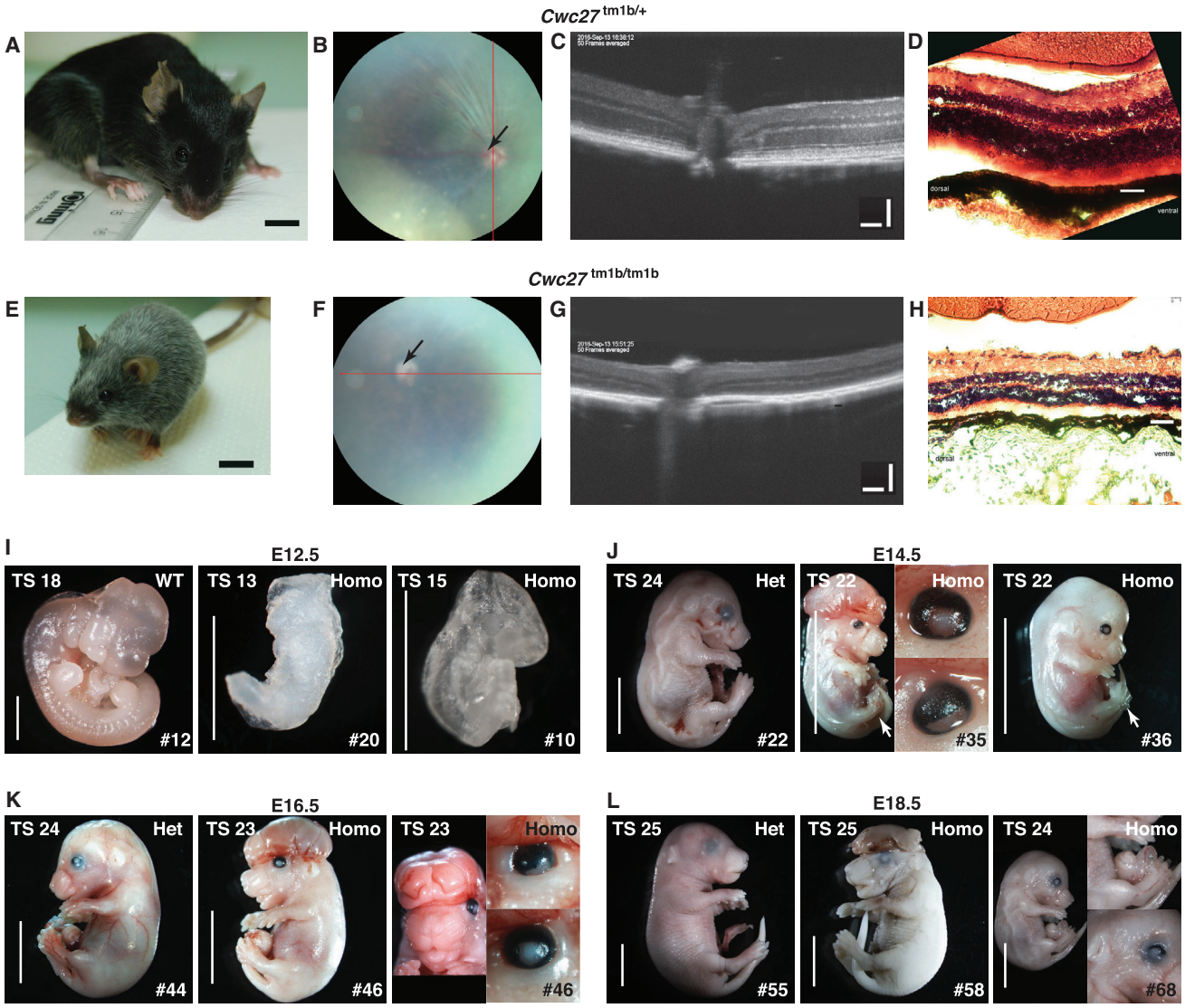

Figure 3. *Cwc27*$^{tm1b/tm1b}$ Mice Phenotype Analysis

(A–H) The overall appearance (A and E), OCT scanning locations (B and F), OCT images (C and G), and H&E staining results (D and H) of *Cwc27*$^{tm1b/+}$ and *Cwc27*$^{tm1b/tm1b}$ mice. The red lines in (B) and (F) indicate the OCT scanning section site. Arrows in (B) and (F) indicate optic discs. Note the retarded growth and severely dystrophic photoreceptor layer in the *Cwc27*$^{tm1b/tm1b}$ mouse. Scale bars represent 6 mm (A and E), 80 μm (C and G), and 35 μm (B and F).

(I–L) Photographs of mouse embryos at E12.5 (I), E14.5 (J), E16.5 (K), and E18.5 (L). Representative specimens of either wild-type or *Cwc27*$^{tm1b/+}$ embryos were used to illustrate normal developmental state. At E12.5, some *Cwc27*$^{tm1b/tm1b}$ embryos (#20 and #10) have neural tube closure failure and limb buds failed to develop. From E14.5 to E18.5, some *Cwc27*$^{tm1b/tm1b}$ embryos present exencephaly (#35, #46, and #58) as well as iris and eyelid malformation (#35, #46, and #68). They also show delays in digit development (#35 and #36, indicated by arrows). An omphalocele, reminiscent of umbilical hernia, was also seen (#68). *Cwc27*$^{tm1b/tm1b}$ embryos are generally less advanced in developmental stage with delay of one or more Theiler stages compared to control littermates. Abbreviations are as follows: WT, wild-type; Het, *Cwc27*$^{tm1b/+}$; Homo, *Cwc27*$^{tm1b/tm1b}$; TS, Theiler staging criteria for mouse development; # indicates numbering of the embryo. Scale bar at E12.5 represents 1 mm. Scale bars at E14.5 to E18.5 represent 5 mm.

quantification results in mice and humans are consistent and demonstrate the incomplete NMD of *Cwc27/CWC27* mRNA for the mutant alleles tested.

Discussion

CWC27 (SDCCAG10) is a peptidyl-prolyl *cis-trans* isomerase (PPIase) found to be associated with spliceosome complexes by multiple proteomic characterization studies.[38–40] PPIases are responsible for inducing protein conformational changes by catalyzing the *cis-trans* isomerization of the peptide bond that precedes proline residues.[41] During splicing reactions, the structure and composition of spliceosome complexes change rapidly, and PPIases may serve as molecular chaperones to assist in this task.[42,43] Interestingly, structural and phylogenetic analysis show that the PPIase activity-determining residue at position 122 in CWC27 has evolved from tryptophan in protists to glutamate in most animals including human,

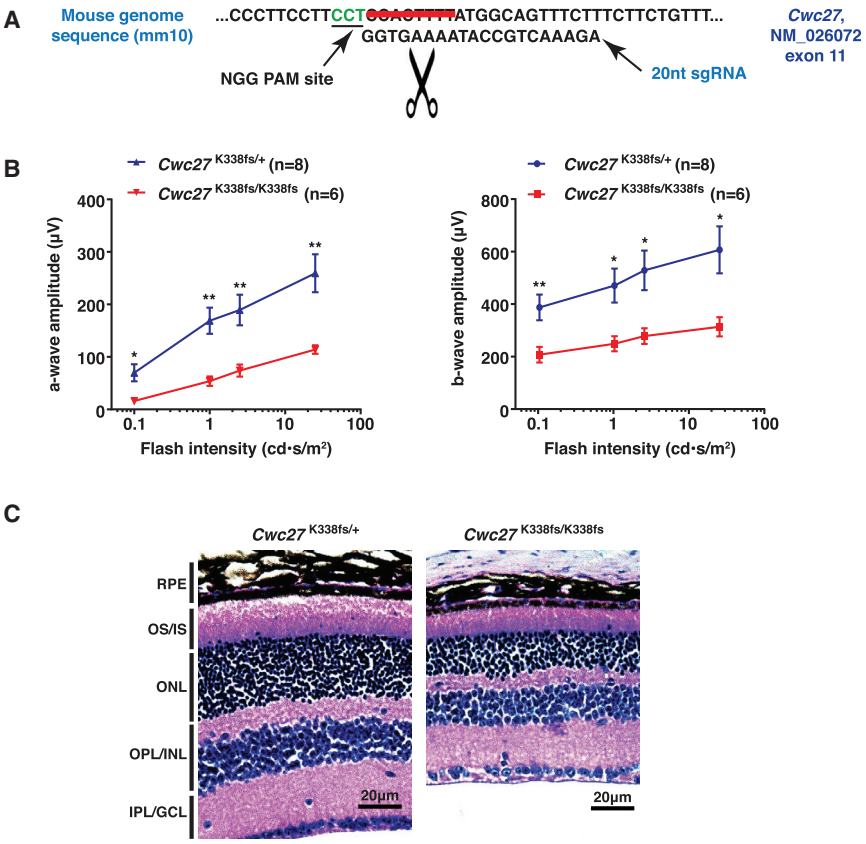

Figure 4. Phenotype Analysis of *Cwc27*$^{K338fs/K338fs}$ Mice

(A) The CRISPR-Cas9 system was used to generate mice with mutant alleles in *Cwc27* exon 11. A 20-nt-long sgRNA sequence was designed to target the indicated region in *Cwc27* exon 11. The scissor indicates the theoretical Cas9 cutting site. The strikethrough indicates the 8 bp deleted in the mouse allele selected for further study (GenBank: NM_026072.1, c.1011_1018delAAAAGTGG [p.Lys338Glyfs*25]).

(B) ERG results show about 50% reduction of a-wave (left) and b-wave (right) response level in *Cwc27*$^{K338fs/K338fs}$ mice (n = 6) compared to *Cwc27*$^{K338fs/+}$ controls (n = 8), indicating compromised retina function. Error bars indicate standard error of the mean. *$p < 0.05$; **$p < 0.01$.

(C) H&E staining shows thinning of outer retina in *Cwc27*$^{K338fs/K338fs}$ mice at the age of 6 months, suggesting photoreceptor degeneration.

suggesting that CWC27 has probably lost its isomerase activity but maintains the proline-binding ability.[43,44] Nevertheless, as a proline binder, CWC27 may mediate protein-protein interactions during the assembly and rearrangement of spliceosome components.[43]

Despite detailed structural data on CWC27, its function in splicing remains undefined. Yeast Cwc27p was recently shown to directly interact with Prp8p (human PRPF8 homolog) and Brr2p (human SNRNP200 homolog) in the spliceosome B^{act} complex.[45] The association of CWC27/Cwc27p with the spliceosomal B^{act} complex and dissociation from the B* complex suggest its role in transitioning the spliceosome from the pre-catalytic to catalytic state.[38,39,45] However, complete disruption of CWC27/Cwc27p homologs in model organisms shows relatively milder phenotype than knockout of several other core splicing factors. Genetic and biochemical studies in yeast have shown that Cwc27p is not required for growth under normal conditions or for the splicing of model substrates in vitro.[46–48] Similarly, *Cwc27* KO mice show relatively late embryonic lethality with a few surviving postnatal mutants instead of being completely early embryonic lethal as observed in other mouse models lacking core splicing factors such as PRPF31,[49] PRPF3,[50] and SNRNP200 (MGI and International Mouse Phenotyping Consortium, IMPC). Further genetic and biochemical studies are warranted to explore the possible explanations for this observation. For example, CWC27 may control the splicing of fewer introns compared with other core splicing factors, or other proteins may compensate for the loss of CWC27 function.

In the present study, we observed a trend for the more N-terminal CWC27 truncations to be associated with more severe phenotypes (Figure 6A). In mice, disruption of exon 1 (tm1Lex) or exon 3 (tm1b) resulted in a wide range of developmental abnormalities with nearly complete embryonic lethality, while the mice with a homozygous frameshift mutation in exon 11 display a late-onset retinal degeneration phenotype. Similarly, the affected individuals in families 3 and 7 with a frameshift mutation (p.Val335Serfs*13) in the C-terminal part of the protein have a milder phenotype, whereas affected individuals with earlier CWC27 protein truncations have craniofacial defects, brachydactyly, short stature, and neurological defects as common features. We have shown that in the affected individuals of family 4 and *Cwc27*$^{K338fs/K338fs}$ mice, *CWC27*/*Cwc27* mRNA does not undergo complete NMD. Thus, the residual function retained by the truncated protein may influence the phenotypic severity. In human CWC27, ten residues (Arg56, Phe61, Ile62, Gln64, Ala102, Asn103, Phe114, Glu122, Leu123, and His127) form the critical proline-binding pocket.[43,44] All of these essential residues are proximal to the protein-truncation site in human affected individuals, with the exception of p.Gln7* in families 5 and 6 (Figure 6A). However, this is a compound heterozygous allele with p.Arg143*, which may still retain residual function. Hence, it is tempting to speculate that the N-terminal proline binding region is critical for CWC27 function, while the C-terminal coiled-coil domain is perhaps less essential, and its disruption leads to milder splicing defects not tolerated primarily

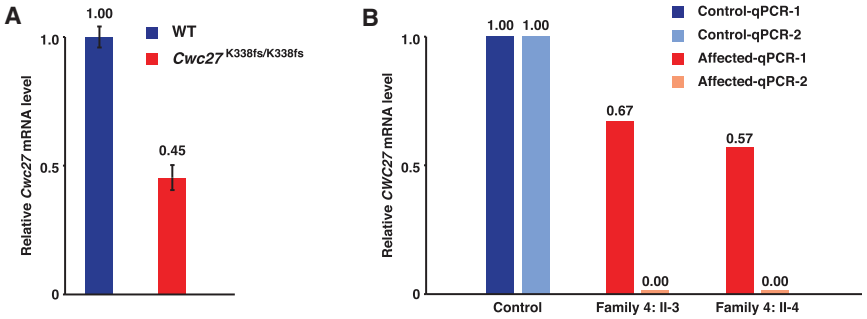

Figure 5. Cwc27/*CWC27* mRNA Does Not Undergo Complete Nonsense-Mediated Decay in Mice and Humans

(A) Quantitative RT-PCR of mouse retina RNA shows the *Cwc27* mRNA level in *Cwc27*$^{K338fs/K338fs}$ is 45% of that in WT mice. Error bars indicate standard error of the mean (n = 4 for each genotype, biological replicates).

(B) Quantitative RT-PCR of human fibroblast RNA shows that the *CWC27* mRNA level in the two affected individuals from family 4 is reduced by 33%–43% compared with the control. qPCR-1 amplifies a region of the *CWC27* mRNA unaffected by the family 4 splice site mutation (exons 1–3). qPCR-2 serves as the negative control and amplifies *CWC27* mRNA between exons 6 and 8, with the exon 6 primer falling in a region that is skipped in the affected individuals from family 4.

in the retina, as shown in the affected individuals from families 3 and 7 as well as the CRISPR-Cas9 mice with late-onset retinal degeneration. Nevertheless, the *CWC27*-associated genotype-phenotype correlation needs to be further delineated by additional genetic analysis in humans or animal models and biochemical studies focusing on the putative CWC27 truncated proteins. The partial NMD escape of *CWC27* mRNA also demonstrates the complexity of NMD mechanism beyond the canonical 50 nt rule.[51,52]

As a splicing factor linked to human disease, *CWC27* is special in two aspects. First, most previously identified

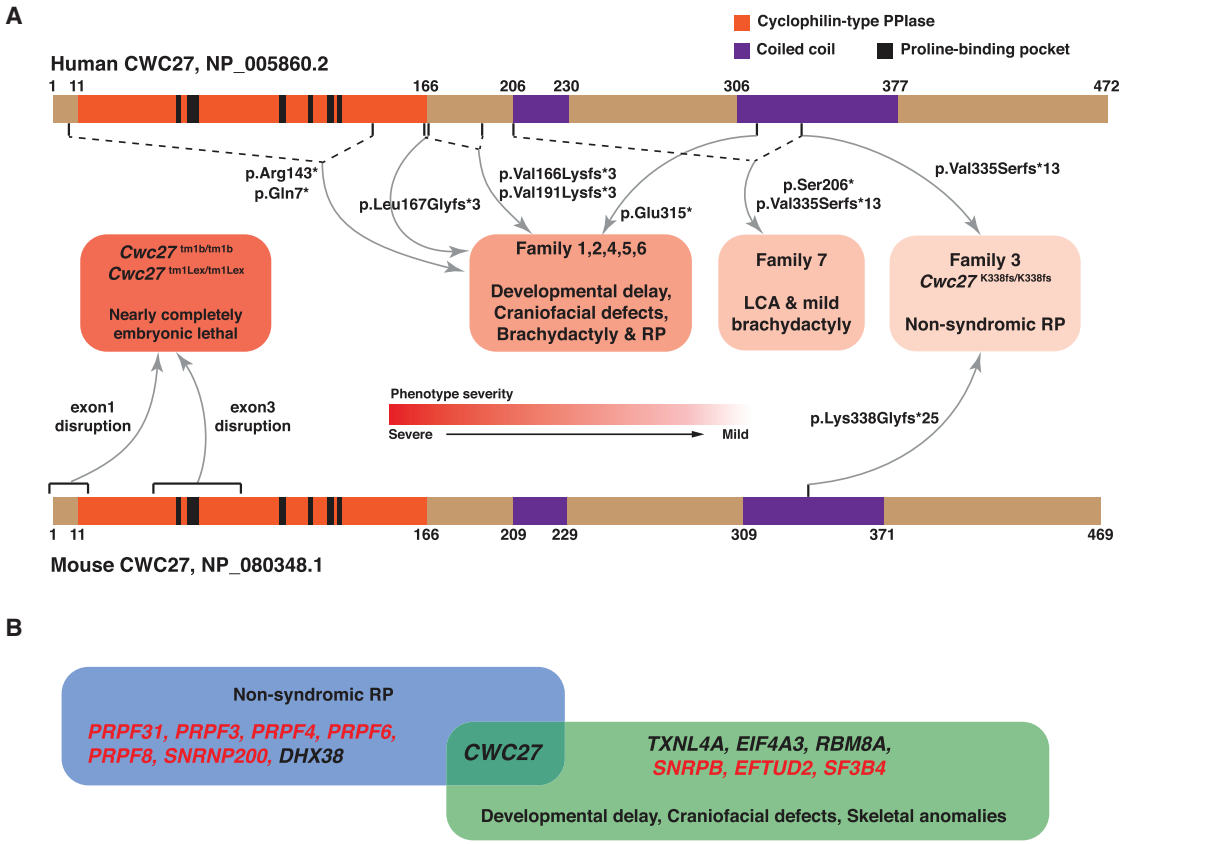

Figure 6. *CWC27*/*Cwc27*-Associated Genotype-Phenotype Correlation and the Uniqueness of *CWC27* among Disease-Associated Spliceosomal Genes

(A) The genotype-phenotype correlation of CWC27 protein defects in humans and mice. Human CWC27 (GenPept: NP_005860.2), mouse CWC27 (GenPept: NP_080348.1), and different phenotype severity groups are presented. Dashed lines indicate compound heterozygous combination of alleles in affected individuals. Note the severity gradient from severe to mild corresponding to the CWC27 variant position from N- to C-terminal.

(B) *CWC27* mutations lead to an autosomal-recessive phenotype covering both non-syndromic RP and early craniofacial/skeletal defects, thus making it a unique member among disease-associated spliceosomal genes. Red font indicates genes with dominant inheritance pattern, while black font indicates recessive inheritance.

spliceosomopathy-associated genes exhibit a dominant inheritance pattern,[53,54] whereas *CWC27* mutations show recessive inheritance (Figure 6B). This suggests that, unlike several other core snRNP components, CWC27 might be an auxiliary factor predicted to function as a chaperone in the spliceosome complex, with single copy abnormality being tolerated. Second, retinal degeneration and craniofacial/skeletal developmental defects are two known non-overlapping spliceosomopathy phenotype groups,[53,54] potentially due to tissue-specific roles for those core spliceosome components. Strikingly, the *CWC27*-associated phenotype is a spliceosome-related Mendelian disorder encompassing both retinal degeneration and craniofacial/skeletal developmental defects (Figure 6B). This implies that CWC27 exerts functions essential for both early tissue development and later functional maintenance. Furthermore, the non-syndromic RP-affected case subject in family 3 also shows that the mature retina, with a high rate of protein turnover and extensive alternative splicing,[55–57] is particularly vulnerable to perturbations of spliceosome assembly and functions. In addition, we observed some family-specific symptoms outside the above-mentioned two phenotypic domains, such as ectodermal defects in family 4 and internal organ anomalies in families 5 and 6, suggesting that CWC27 may play important roles in additional tissues.

To conclude, we have identified *CWC27* mutations as the molecular etiology of an autosomal-recessive disorder characterized by a spectrum of phenotypes including retinal degeneration, brachydactyly, craniofacial defects, short stature, and neurological defects. This disease phenotype, together with its genetic underpinnings and biochemical implications, paves the way for further understanding of the pathological mechanisms that arise upon disruption of splicing components.

Supplemental Data

Supplemental Data include two tables and can be found with this article online at http://dx.doi.org/10.1016/j.ajhg.2017.02.008.

Consortia

The UK Inherited Retinal Dystrophy Consortium includes Graeme Black, Georgina Hall, Rachel Gillespie, Simon Ramsden, Forbes Manson, Panagiotis Sergouniotis, Chris Inglehearn, Carmel Toomes, Manir Ali, Martin McKibbin, James Poulter, Emma Lord, Andrea Nemeth, Stephanie Halford, Susan Downes, and Jing Yu.

Acknowledgments

We thank the affected individuals and their family members for participating in our study. This work was supported by grants from RP Fighting Blindness (UK), Fight for Sight, Moorfields Eye Charity, Moorfields Special Trustees, Foundation Fighting Blindness(CD-CL-0711-0518-UCL), the National Institute for Health Research Biomedical Research Centre at Moorfields Eye Hospital, National Health Service Foundation Trust, and UCL Institute of Ophthalmology (A.J.H., M.E.C., M.M., and A.R.W.), grants from National Eye Institute (R01EY022356, R01EY018571, EY002520), Retinal Research Foundation, Foundation Fighting Blindness (BR-GE-0613-0618-BCM), and NIH shared instrument grant 1S10RR026550 to R.C., grants from National Eye Institute (R01EY020551) to J.v.L., funding from the Agence Nationale de la Recherche (ANR-10-IAHU-01, CranioRespiro) to S.L., C.T.G., and J.A., grants ANR-10-LABX-54 MEMOLIFE and ANR-11-IDEX-0001-02 PSL* Research University to V.B. and H.L.H., grants from National Eye Institute (EY021163, EY019861, and EY019007 Core Support for Vision Research) and unrestricted funds from Research to Prevent Blindness (New York, NY) to R.A., grants from the Foundation Fighting Blindness (CD-CL-0808-0470-PUMCH and CD-CL-0214-0631-PUMCH), the Ministry of Science and Technology of the People's Republic of China (grant 2010DFB33430), National Natural Science Foundation of China (81470669), and Beijing Natural Science Foundation (7152116) to R.S., and grants PI13/0226 from Spanish ISCIII, Madrid, Spain and ONCE. We also thank Blanca Garcia-Sandoval from Department of Ophthalmology of IIS-FJD, Madrid, Spain for help on this project.

Received: December 17, 2016
Accepted: February 15, 2017
Published: March 9, 2017

Web Resources

1000 Genomes, http://www.internationalgenome.org/
CHARGE Consortium, http://www.chargeconsortium.com/
ExAC Browser, http://exac.broadinstitute.org/
GenBank, http://www.ncbi.nlm.nih.gov/genbank/
GeneMatcher, https://genematcher.org/
gnomAD Browser, http://gnomad.broadinstitute.org/
HGMD, http://www.hgmd.cf.ac.uk/
International Mouse Phenotyping Consortium, http://www.mousephenotype.org/
Knockout Mouse Project (KOMP) Repository, https://www.komp.org/
MMRRC, http://mmrrc.mousebiology.org/phenotype/
Mouse Genome Informatics, http://www.informatics.jax.org/
NHLBI Exome Sequencing Project (ESP) Exome Variant Server, http://evs.gs.washington.edu/EVS/
OMIM, http://www.omim.org/
Optimized CRISPR Design, http://crispr.mit.edu/

References

1. Pan, Q., Shai, O., Lee, L.J., Frey, B.J., and Blencowe, B.J. (2008). Deep surveying of alternative splicing complexity in the human transcriptome by high-throughput sequencing. Nat. Genet. *40*, 1413–1415.
2. Wang, E.T., Sandberg, R., Luo, S., Khrebtukova, I., Zhang, L., Mayr, C., Kingsmore, S.F., Schroth, G.P., and Burge, C.B. (2008). Alternative isoform regulation in human tissue transcriptomes. Nature *456*, 470–476.
3. Matera, A.G., and Wang, Z. (2014). A day in the life of the spliceosome. Nat. Rev. Mol. Cell Biol. *15*, 108–121.
4. Jurica, M.S., and Moore, M.J. (2003). Pre-mRNA splicing: awash in a sea of proteins. Mol. Cell *12*, 5–14.

5. Rappsilber, J., Ryder, U., Lamond, A.I., and Mann, M. (2002). Large-scale proteomic analysis of the human spliceosome. Genome Res. *12*, 1231–1245.
6. Zhou, Z., Licklider, L.J., Gygi, S.P., and Reed, R. (2002). Comprehensive proteomic analysis of the human spliceosome. Nature *419*, 182–185.
7. Korneta, I., Magnus, M., and Bujnicki, J.M. (2012). Structural bioinformatics of the human spliceosomal proteome. Nucleic Acids Res. *40*, 7046–7065.
8. Wieczorek, D., Newman, W.G., Wieland, T., Berulava, T., Kaffe, M., Falkenstein, D., Beetz, C., Graf, E., Schwarzmayr, T., Douzgou, S., et al. (2014). Compound heterozygosity of low-frequency promoter deletions and rare loss-of-function mutations in TXNL4A causes Burn-McKeown syndrome. Am. J. Hum. Genet. *95*, 698–707.
9. Albers, C.A., Paul, D.S., Schulze, H., Freson, K., Stephens, J.C., Smethurst, P.A., Jolley, J.D., Cvejic, A., Kostadima, M., Bertone, P., et al. (2012). Compound inheritance of a low-frequency regulatory SNP and a rare null mutation in exon-junction complex subunit RBM8A causes TAR syndrome. Nat. Genet. *44*, 435–439, S1–S2.
10. Lynch, D.C., Revil, T., Schwartzentruber, J., Bhoj, E.J., Innes, A.M., Lamont, R.E., Lemire, E.G., Chodirker, B.N., Taylor, J.P., Zackai, E.H., et al.; Care4Rare Canada (2014). Disrupted auto-regulation of the spliceosomal gene SNRPB causes cerebro-costo-mandibular syndrome. Nat. Commun. *5*, 4483.
11. Favaro, F.P., Alvizi, L., Zechi-Ceide, R.M., Bertola, D., Felix, T.M., de Souza, J., Raskin, S., Twigg, S.R., Weiner, A.M., Armas, P., et al. (2014). A noncoding expansion in EIF4A3 causes Richieri-Costa-Pereira syndrome, a craniofacial disorder associated with limb defects. Am. J. Hum. Genet. *94*, 120–128.
12. Lines, M.A., Huang, L., Schwartzentruber, J., Douglas, S.L., Lynch, D.C., Beaulieu, C., Guion-Almeida, M.L., Zechi-Ceide, R.M., Gener, B., Gillessen-Kaesbach, G., et al.; FORGE Canada Consortium (2012). Haploinsufficiency of a spliceosomal GTPase encoded by EFTUD2 causes mandibulofacial dysostosis with microcephaly. Am. J. Hum. Genet. *90*, 369–377.
13. Bernier, F.P., Caluseriu, O., Ng, S., Schwartzentruber, J., Buckingham, K.J., Innes, A.M., Jabs, E.W., Innis, J.W., Schuette, J.L., Gorski, J.L., et al.; FORGE Canada Consortium (2012). Haploinsufficiency of SF3B4, a component of the pre-mRNA spliceosomal complex, causes Nager syndrome. Am. J. Hum. Genet. *90*, 925–933.
14. Chakarova, C.F., Hims, M.M., Bolz, H., Abu-Safieh, L., Patel, R.J., Papaioannou, M.G., Inglehearn, C.F., Keen, T.J., Willis, C., Moore, A.T., et al. (2002). Mutations in HPRP3, a third member of pre-mRNA splicing factor genes, implicated in autosomal dominant retinitis pigmentosa. Hum. Mol. Genet. *11*, 87–92.
15. Vithana, E.N., Abu-Safieh, L., Allen, M.J., Carey, A., Papaioannou, M., Chakarova, C., Al-Maghtheh, M., Ebenezer, N.D., Willis, C., Moore, A.T., et al. (2001). A human homolog of yeast pre-mRNA splicing gene, PRP31, underlies autosomal dominant retinitis pigmentosa on chromosome 19q13.4 (RP11). Mol. Cell *8*, 375–381.
16. Chen, X., Liu, Y., Sheng, X., Tam, P.O., Zhao, K., Chen, X., Rong, W., Liu, Y., Liu, X., Pan, X., et al. (2014). PRPF4 mutations cause autosomal dominant retinitis pigmentosa. Hum. Mol. Genet. *23*, 2926–2939.
17. Tanackovic, G., Ransijn, A., Ayuso, C., Harper, S., Berson, E.L., and Rivolta, C. (2011). A missense mutation in PRPF6 causes impairment of pre-mRNA splicing and autosomal-dominant retinitis pigmentosa. Am. J. Hum. Genet. *88*, 643–649.
18. McKie, A.B., McHale, J.C., Keen, T.J., Tarttelin, E.E., Goliath, R., van Lith-Verhoeven, J.J., Greenberg, J., Ramesar, R.S., Hoyng, C.B., Cremers, F.P., et al. (2001). Mutations in the pre-mRNA splicing factor gene PRPC8 in autosomal dominant retinitis pigmentosa (RP13). Hum. Mol. Genet. *10*, 1555–1562.
19. Zhao, C., Bellur, D.L., Lu, S., Zhao, F., Grassi, M.A., Bowne, S.J., Sullivan, L.S., Daiger, S.P., Chen, L.J., Pang, C.P., et al. (2009). Autosomal-dominant retinitis pigmentosa caused by a mutation in SNRNP200, a gene required for unwinding of U4/U6 snRNAs. Am. J. Hum. Genet. *85*, 617–627.
20. Papasaikas, P., and Valcárcel, J. (2016). The spliceosome: the ultimate RNA chaperone and sculptor. Trends Biochem. Sci. *41*, 33–45.
21. Salvo, J., Lyubasyuk, V., Xu, M., Wang, H., Wang, F., Nguyen, D., Wang, K., Luo, H., Wen, C., Shi, C., et al. (2015). Next-generation sequencing and novel variant determination in a cohort of 92 familial exudative vitreoretinopathy patients. Invest. Ophthalmol. Vis. Sci. *56*, 1937–1946.
22. Xu, M., Gelowani, V., Eblimit, A., Wang, F., Young, M.P., Sawyer, B.L., Zhao, L., Jenkins, G., Creel, D.J., Wang, K., et al. (2015). ATF6 is mutated in early onset photoreceptor degeneration with macular involvement. Invest. Ophthalmol. Vis. Sci. *56*, 3889–3895.
23. Tajiguli, A., Xu, M., Fu, Q., Yiming, R., Wang, K., Li, Y., Eblimit, A., Sui, R., Chen, R., and Aisa, H.A. (2016). Next-generation sequencing-based molecular diagnosis of 12 inherited retinal disease probands of Uyghur ethnicity. Sci. Rep. *6*, 21384.
24. Li, H., and Durbin, R. (2009). Fast and accurate short read alignment with Burrows-Wheeler transform. Bioinformatics *25*, 1754–1760.
25. McKenna, A., Hanna, M., Banks, E., Sivachenko, A., Cibulskis, K., Kernytsky, A., Garimella, K., Altshuler, D., Gabriel, S., Daly, M., and DePristo, M.A. (2010). The Genome Analysis Toolkit: a MapReduce framework for analyzing next-generation DNA sequencing data. Genome Res. *20*, 1297–1303.
26. Challis, D., Yu, J., Evani, U.S., Jackson, A.R., Paithankar, S., Coarfa, C., Milosavljevic, A., Gibbs, R.A., and Yu, F. (2012). An integrative variant analysis suite for whole exome next-generation sequencing data. BMC Bioinformatics *13*, 8.
27. Lek, M., Karczewski, K.J., Minikel, E.V., Samocha, K.E., Banks, E., Fennell, T., O'Donnell-Luria, A.H., Ware, J.S., Hill, A.J., Cummings, B.B., et al.; Exome Aggregation Consortium (2016). Analysis of protein-coding genetic variation in 60,706 humans. Nature *536*, 285–291.
28. Psaty, B.M., O'Donnell, C.J., Gudnason, V., Lunetta, K.L., Folsom, A.R., Rotter, J.I., Uitterlinden, A.G., Harris, T.B., Witteman, J.C., Boerwinkle, E.; and CHARGE Consortium (2009). Cohorts for Heart and Aging Research in Genomic Epidemiology (CHARGE) Consortium: Design of prospective meta-analyses of genome-wide association studies from 5 cohorts. Circ Cardiovasc Genet *2*, 73–80.
29. Tennessen, J.A., Bigham, A.W., O'Connor, T.D., Fu, W., Kenny, E.E., Gravel, S., McGee, S., Do, R., Liu, X., Jun, G., et al.; Broad GO; Seattle GO; and NHLBI Exome Sequencing Project (2012). Evolution and functional impact of rare coding variation from deep sequencing of human exomes. Science *337*, 64–69.

30. Abecasis, G.R., Altshuler, D., Auton, A., Brooks, L.D., Durbin, R.M., Gibbs, R.A., Hurles, M.E., McVean, G.A.; and 1000 Genomes Project Consortium (2010). A map of human genome variation from population-scale sequencing. Nature *467*, 1061–1073.
31. Wang, K., Li, M., and Hakonarson, H. (2010). ANNOVAR: functional annotation of genetic variants from high-throughput sequencing data. Nucleic Acids Res. *38*, e164.
32. Liu, X., Jian, X., and Boerwinkle, E. (2011). dbNSFP: a lightweight database of human nonsynonymous SNPs and their functional predictions. Hum. Mutat. *32*, 894–899.
33. Marcelli, F., Escher, P., and Schorderet, D.F. (2012). Exploration of the visual system: part 2: in vivo analysis methods: virtual-reality optomotor system, fundus examination, and fluorescent angiography. Curr. Protoc. Mouse Biol. *2*, 207–218.
34. Livak, K.J., and Schmittgen, T.D. (2001). Analysis of relative gene expression data using real-time quantitative PCR and the 2(-Delta Delta C(T)) Method. Methods *25*, 402–408.
35. Lorda-Sanchez, I., Trujillo, M.J., Gimenez, A., Garcia-Sandoval, B., Franco, A., Sanz, R., Rodriguez de Alba, M., Ramos, C., and Ayuso, C. (1999). Retinitis pigmentosa, mental retardation, marked short stature, and brachydactyly in two sibs. Ophthalmic Genet. *20*, 127–131.
36. Jian, X., Boerwinkle, E., and Liu, X. (2014). In silico prediction of splice-altering single nucleotide variants in the human genome. Nucleic Acids Res. *42*, 13534–13544.
37. Mattapallil, M.J., Wawrousek, E.F., Chan, C.C., Zhao, H., Roychoudhury, J., Ferguson, T.A., and Caspi, R.R. (2012). The Rd8 mutation of the Crb1 gene is present in vendor lines of C57BL/6N mice and embryonic stem cells, and confounds ocular induced mutant phenotypes. Invest. Ophthalmol. Vis. Sci. *53*, 2921–2927.
38. Fabrizio, P., Dannenberg, J., Dube, P., Kastner, B., Stark, H., Urlaub, H., and Lührmann, R. (2009). The evolutionarily conserved core design of the catalytic activation step of the yeast spliceosome. Mol. Cell *36*, 593–608.
39. Hegele, A., Kamburov, A., Grossmann, A., Sourlis, C., Wowro, S., Weimann, M., Will, C.L., Pena, V., Lührmann, R., and Stelzl, U. (2012). Dynamic protein-protein interaction wiring of the human spliceosome. Mol. Cell *45*, 567–580.
40. Jurica, M.S., Licklider, L.J., Gygi, S.R., Grigorieff, N., and Moore, M.J. (2002). Purification and characterization of native spliceosomes suitable for three-dimensional structural analysis. RNA *8*, 426–439.
41. Fischer, G., Bang, H., and Mech, C. (1984). [Determination of enzymatic catalysis for the cis-trans-isomerization of peptide binding in proline-containing peptides]. Biomed. Biochim. Acta *43*, 1101–1111.
42. Ingelfinger, D., Göthel, S.F., Marahiel, M.A., Reidt, U., Ficner, R., Lührmann, R., and Achsel, T. (2003). Two protein-protein interaction sites on the spliceosome-associated human cyclophilin CypH. Nucleic Acids Res. *31*, 4791–4796.
43. Ulrich, A., and Wahl, M.C. (2014). Structure and evolution of the spliceosomal peptidyl-prolyl cis-trans isomerase Cwc27. Acta Crystallogr. D Biol. Crystallogr. *70*, 3110–3123.
44. Davis, T.L., Walker, J.R., Campagna-Slater, V., Finerty, P.J., Paramanathan, R., Bernstein, G., MacKenzie, F., Tempel, W., Ouyang, H., Lee, W.H., et al. (2010). Structural and biochemical characterization of the human cyclophilin family of peptidyl-prolyl isomerases. PLoS Biol. *8*, e1000439.
45. Yan, C., Wan, R., Bai, R., Huang, G., and Shi, Y. (2016). Structure of a yeast activated spliceosome at 3.5 Å resolution. Science *353*, 904–911.
46. Giaever, G., Chu, A.M., Ni, L., Connelly, C., Riles, L., Véronneau, S., Dow, S., Lucau-Danila, A., Anderson, K., André, B., et al. (2002). Functional profiling of the *Saccharomyces cerevisiae* genome. Nature *418*, 387–391.
47. Winzeler, E.A., Shoemaker, D.D., Astromoff, A., Liang, H., Anderson, K., Andre, B., Bangham, R., Benito, R., Boeke, J.D., Bussey, H., et al. (1999). Functional characterization of the *S. cerevisiae* genome by gene deletion and parallel analysis. Science *285*, 901–906.
48. Ohrt, T., Prior, M., Dannenberg, J., Odenwälder, P., Dybkov, O., Rasche, N., Schmitzová, J., Gregor, I., Fabrizio, P., Enderlein, J., and Lührmann, R. (2012). Prp2-mediated protein rearrangements at the catalytic core of the spliceosome as revealed by dcFCCS. RNA *18*, 1244–1256.
49. Bujakowska, K., Maubaret, C., Chakarova, C.F., Tanimoto, N., Beck, S.C., Fahl, E., Humphries, M.M., Kenna, P.F., Makarov, E., Makarova, O., et al. (2009). Study of gene-targeted mouse models of splicing factor gene Prpf31 implicated in human autosomal dominant retinitis pigmentosa (RP). Invest. Ophthalmol. Vis. Sci. *50*, 5927–5933.
50. Graziotto, J.J., Inglehearn, C.F., Pack, M.A., and Pierce, E.A. (2008). Decreased levels of the RNA splicing factor Prpf3 in mice and zebrafish do not cause photoreceptor degeneration. Invest. Ophthalmol. Vis. Sci. *49*, 3830–3838.
51. Thermann, R., Neu-Yilik, G., Deters, A., Frede, U., Wehr, K., Hagemeier, C., Hentze, M.W., and Kulozik, A.E. (1998). Binary specification of nonsense codons by splicing and cytoplasmic translation. EMBO J. *17*, 3484–3494.
52. Zhang, J., Sun, X., Qian, Y., LaDuca, J.P., and Maquat, L.E. (1998). At least one intron is required for the nonsense-mediated decay of triosephosphate isomerase mRNA: a possible link between nuclear splicing and cytoplasmic translation. Mol. Cell. Biol. *18*, 5272–5283.
53. Mordes, D., Luo, X., Kar, A., Kuo, D., Xu, L., Fushimi, K., Yu, G., Sternberg, P., Jr., and Wu, J.Y. (2006). Pre-mRNA splicing and retinitis pigmentosa. Mol. Vis. *12*, 1259–1271.
54. Lehalle, D., Wieczorek, D., Zechi-Ceide, R.M., Passos-Bueno, M.R., Lyonnet, S., Amiel, J., and Gordon, C.T. (2015). A review of craniofacial disorders caused by spliceosomal defects. Clin. Genet. *88*, 405–415.
55. Wan, J., Masuda, T., Hackler, L., Jr., Torres, K.M., Merbs, S.L., Zack, D.J., and Qian, J. (2011). Dynamic usage of alternative splicing exons during mouse retina development. Nucleic Acids Res. *39*, 7920–7930.
56. Wright, A.F., Chakarova, C.F., Abd El-Aziz, M.M., and Bhattacharya, S.S. (2010). Photoreceptor degeneration: genetic and mechanistic dissection of a complex trait. Nat. Rev. Genet. *11*, 273–284.
57. Murphy, D., Cieply, B., Carstens, R., Ramamurthy, V., and Stoilov, P. (2016). The Musashi 1 controls the splicing of photoreceptor-specific exons in the vertebrate retina. PLoS Genet. *12*, e1006256.